Journal of Materials Chemistry C

PAPER

Efficient and versatile mechanochromic luminescence of phenanthroimidazolylbenzothiadiazoles: tricolor switching and directional control over the chromism

Received 00th January 20xx,
Accepted 00th January 20xx

DOI: 10.1039/x0xx00000x

www.rsc.org/

Sayaka Nagai,[a] Maho Yamashita,[b] Takashi Tachikawa,*[bc] Takashi Ubukata,[a] Masatoshi Asami[a] and Suguru Ito*[a]

Mechanochromic luminescence (MCL) refers to the mechanical-stimuli-responsive reversible color change of solid-state-emissive dyes. In spite of recent extensive studies on the development of MCL dyes, most of these display bicolor MCL that usually manifests in bathochromic shifts of the emission color in response to mechanical stimuli. Herein, phenanthroimidazolylbenzothiadiazoles are described as a new class of highly emissive solid-state fluorophores that exhibit more versatile MCL properties. Depending on the substituent on the phenyl group of the benzothiadiazole ring, bathochromically or hypsochromically shifted bicolor MCL as well as tricolor MCL are observed for these dyes. Powder X-ray diffraction and differential scanning calorimetry measurements for the bicolor MCL systems indicated that the mechanism of the emission-color change upon grinding is based on typical crystalline-to-amorphous phase transitions. To investigate the tricolor MCL system in detail, single-particle-level fluorescence microscopy has been applied for the first time, which allowed distinguishing three states with different emission properties. The versatility of the present MCL system was attributed to the formation of different crystal structures by introducing various substituents on the aforementioned phenyl group. These results provide useful insights into generating diverse MCL dyes in the future and thus promote the practical applications of MCL systems.

Introduction

Solid-state-emissive materials often exhibit mechanochromic luminescence (MCL), i.e., a reversible color change of the solid-state emission induced by exposure to a mechanical stimulus.[1–4] During the past decade, research on organic luminophores with MCL properties has rapidly grown, as this class of materials is expected to constitute the principal components of advanced optical technologies in the areas of information security, pressure sensors, and memory devices. Since the fluorescence quantum yield of typical organic fluorophores decreases significantly in the solid state on account of the concentration quenching, some strategies are required to achieve efficient solid-state emission. Notably, the mechanism of the efficient solid-state emission for most MCL dyes is based on aggregation-induced emission (AIE), in which non-emissive or weakly emissive isolated molecules become emissive upon aggregation.[5,6] However, the luminescence quantum yields of most of the reported MCL dyes are generally < 50%, even if they exhibit AIE behavior. Moreover, the clear majority of typical MCL dyes exhibit a bathochromic shift of the maximum solid-state emission wavelength in response to a mechanical stimulus. It remains a challenging task to achieve both bathochromically and hypsochromically shifted MCL in dyes based on the same molecular scaffold.[7] Another significant challenge in the field of MCL is to realize multicolor luminescence in response to different mechanical stimuli.[8] Therefore, the development of new organic dyes that exhibit multicolor MCL together with high solid-state luminescence quantum yields is particularly desirable both from a fundamental scientific perspective, as well as considering the wealth of potential applications.

We have recently developed indolylbenzothiadiazoles as a new class of non-AIE-type MCL dyes that exhibit bathochromically shifted MCL with self-recovering nature (Fig. 1a).[9] The molecular design is based on the heteroaromatic donor-acceptor (D-A) structure that arises from the direct connection of electron-donating indole and electron-accepting benzothiadiazole rings. Herein, we report the highly emissive non-AIE-type MCL dyes **1a–f**, which use phenanthroimidazole ring[10] as the electron-donating heteroaromatic ring (Fig. 1b). Most remarkably, **1a–f** show not only the typical bathochromically shifted bicolor MCL but also a rare tricolor MCL as well as a hypsochromically shifted MCL, whereby the

[a] *Department of Advanced Materials Chemistry, Graduate School of Engineering, Yokohama National University, 79-5 Tokiwadai, Hodogaya-ku, Yokohama 240-8501, Japan. E-mail: suguru-ito@ynu.ac.jp*
[b] *Department of Chemistry, Graduate School of Science, Kobe University, 1-1 Rokkodai-cho, Nada-ku, Kobe 657-8501, Japan*
[c] *Molecular Photoscience Research Center, Kobe University, 1-1 Rokkodai-cho, Nada-ku, Kobe 657-8501, Japan. E-mail: tachikawa@port.kobe-u.ac.jp*

†Electronic Supplementary Information (ESI) available: Spectral data, photographs of the solvatochromic luminescence, X-ray diffraction analyses, theoretical calculations, and PXRD data. CCDC 1886938 (**1a**), 1886939 (**1b**), 1886940 (**1c**), 1886941 (**1d**), 1886942 (**1e**), and 1886943 (**1f**). See DOI: 10.1039/x0xx00000x

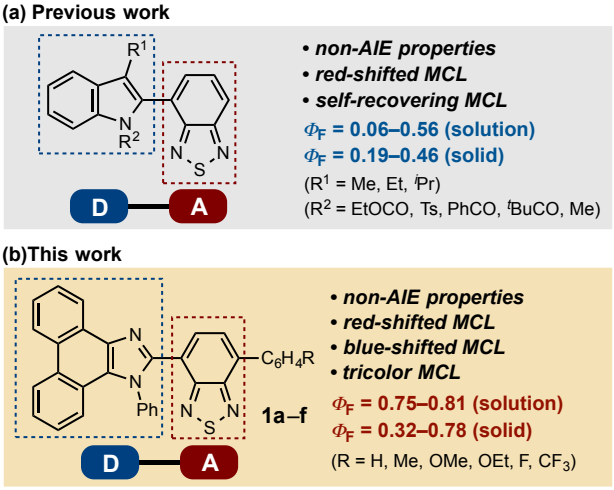

Fig. 1 Structures and properties of previously reported indolylbenzothiadiazoles (a) and phenanthroimidazolylbenzothiadiazoles **1a–f** (b).

specific type of MCL that manifests depends on the substituent on the benzene ring at the 7-position of the benzothiadiazole ring. In addition, single-particle-level observations of the emission properties have been used for the first time to analyze this tricolor MCL system, which allowed clearly distinguishing the three states that exhibit different emission colors.

Results and discussion

Phenanthroimidazolylbenzothiadiazoles **1a–f** were obtained from the Suzuki–Miyaura coupling between bromide **2** and phenylboronic acid derivatives (Scheme 1). Following a literature procedure for the synthesis of 1,2-diaryl-1*H*-phenanthro[9,10-*d*]imidazole,[10j] **2** was prepared in 75% yield by a four-component condensation reaction: a mixture of 9,10-phenanthrenequinone, ammonium acetate, aniline, and 4-bromo-7-formyl-2,1,3-benzothiadiazole in acetic acid was stirred for 12 h at 110 °C. Subsequently, **2** and phenylboronic acid (1.3 equiv) were stirred in the presence of $Pd(PPh_3)_4$ (4 mol%) in refluxing toluene/aqueous K_2CO_3 (1.4 M). Preparative thin-layer chromatography of the resulting crude product furnished **1a** (R = H) in 79% yield. The other

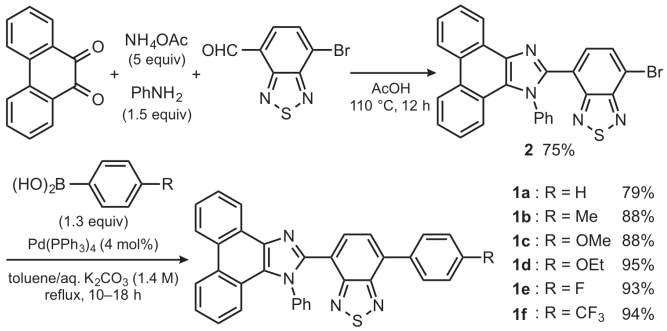

Scheme 1 Synthesis of phenanthroimidazolylbenzothiadiazoles **1a–f**.

derivatives with electron-donating (**1b**: R = Me; **1c**: R = OMe; **1d**: R = OEt) or -withdrawing (**1e**: R = F; **1f**: R = CF_3) substituents on the benzene ring were prepared in a similar fashion (88–95% yield) using 4-substituted phenylboronic acid. Crystalline samples of **1a–f**, obtained from recrystallizations from toluene, were used in the following experiments.

The photophysical properties of **1a–f** in solution (toluene; 1.0×10^{-5} M) and in the solid state are summarized in Table 1. A toluene solution of non-substituted **1a** (R = H) exhibited its maximum absorption band (λ_{abs}) at 414 nm and an intense green emission (λ_{em} = 537 nm) with high fluorescence quantum yield (Φ_F = 0.79). The large Stokes shift (123 nm) and the solvatochromic nature of the fluorescence (Fig. S1) suggested that the maximum absorption band of D–A dye **1a** should be assigned to the intramolecular charge-transfer transition. The solid-state emission of crystalline **1a** was observed in the same region [λ_{em} = 526 nm; $\Delta\lambda_{em}$ = λ_{em} (crystal) – λ_{em} (toluene) = –11 nm] under retention of the high fluorescence quantum yield (Φ_F = 0.60). Similarly, the substituted derivatives **1b–f** showed good to high fluorescence quantum yields both in toluene (Φ_F = 0.75–0.81) and in the crystalline state (Φ_F = 0.32–0.78). Regarding the emission color of **1a–f**, the maximum emission bands of all derivatives appeared in the same green region (λ_{em} = 537–550 nm) in toluene, irrespective of the substituent R on the benzene ring, whereas those of the crystalline samples were observed in a wider region (λ_{em} = 505–607 nm). The differences between the emission maxima of the toluene solutions and those of the crystalline samples are relatively small for **1a**, **1b**, **1d**, and **1f**

Table 1 Photophysical properties of phenanthroimidazolylbenzothiadiazoles **1a–f**.

		Absorption in toluene	Fluorescence in toluene[b]		Fluorescence of a crystalline sample[b]		Difference of emission maximum	Fluorescence of a ground sample[b]	
Compd.	R	λ_{abs} (nm)[a]	λ_{em} (nm)	Φ_F[d]	λ_{em} (nm)	Φ_F[d]	$\Delta\lambda_{em}$ (nm)[c]	λ_{em} (nm)	Φ_F[d]
1a	H	414	537	0.79	526	0.60	–11	565	0.54
1b	Me	413	538	0.81	545	0.78	+7	570	0.72
1c	OMe	419	549	0.79	607	0.33	+58	581	0.67
1d	OEt	417	549	0.79	553	0.53	+4	573	0.54
1e	F	416	541	0.77	505	0.61	–36	567	0.60
1f	CF_3	420	550	0.75	535	0.32	–15	566	0.60

[a] Maximum absorption bands (λ_{abs} > 350 nm) in toluene (1.0×10^{-5} M). [b] Maximum emission bands (λ_{em}) and absolute quantum yields (Φ_F) in toluene (1.0×10^{-5} M), in crystalline powdered form, and in ground amorphous form. [c] $\Delta\lambda_{em}$ = λ_{em} (crystal) – λ_{em} (toluene). [d] Absolute quantum yields were measured using an integrating sphere.

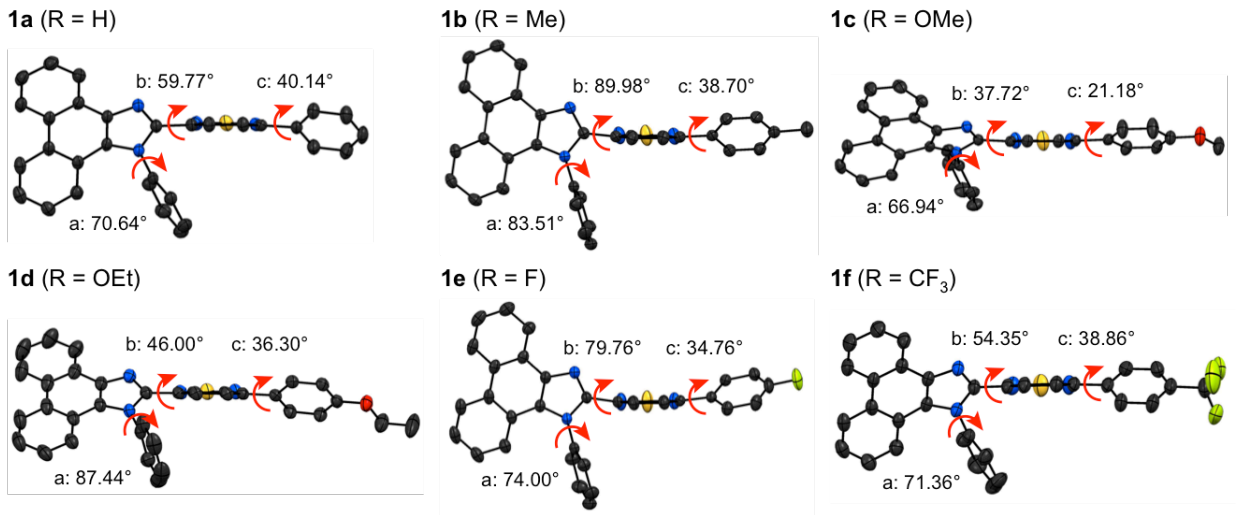

Fig. 2 Molecular structures of **1a–f** with thermal ellipsoids at 50% probability. All hydrogen atoms are omitted for clarity. Color code: gray = C; red = O; blue = N; yellow = S; green = F.

($\Delta\lambda_{em}$ = ±15 nm). Conversely, the emission maxima of methoxy-substituted **1c** and fluoro-substituted **1e** in the crystalline state are significantly shifted in bathochromic ($\Delta\lambda_{em}$ = +58 nm) and hypsochromic direction ($\Delta\lambda_{em}$ = –36 nm), respectively, compared to those of their toluene solutions. Since other, structurally related derivatives with electron-donating and -withdrawing substituents (**1d**: R = OEt; **1f**: R = CF_3) do not exhibit such substantial shifts, the emission wavelengths of crystalline **1a–f** should be affected by the difference in their molecular conformation rather than by the electron-donating or -withdrawing nature of the substituent R.

The molecular structures of **1a–f** in the crystalline state were determined by single-crystal X-ray diffraction analyses (Fig. 2 and S2–S7). The conformation of tetra(hetero)aryl compounds **1a–f** is characterized by the three dihedral angles a–c of adjacent (hetero)aryl groups, which are considerably different in **1a–f** (Fig. 2). The sum of the three dihedral angles for each compound, which indicates the planarity of the molecular structure, is summarized in Table 2 (**1a**: 170.55°; **1b**: 212.19°; **1c**: 125.84°; **1d**: 169.74°; **1e**: 188.52°; **1f**: 164.57°), together with the difference of the emission maxima ($\Delta\lambda_{em}$) in the crystalline state and in solution. Methoxy-substituted **1c**, which exhibits the largest $\Delta\lambda_{em}$ value of +58 nm, exhibits also the most planar structure (a+b+c = 125.84°) among **1a–f**, indicating that a planar structure should contribute to the bathochromically shifted emission of **1c** in the crystalline state. Another important structural characteristic of these compounds is that the benzothiadiazole ring of some of the investigated compounds shows a pronounced bent structure on account of the tight crystal packing. A comparison of the bend angles of the benzothiadiazole rings in **1a–f** (Table 2, Fig. S8) revealed that fluoro-substituted **1e** exhibits the most distorted benzothiadiazole ring (bend angle = 12.11°), which should account for the largest hypsochromic shift of the emission of crystalline **1e** ($\Delta\lambda_{em}$ = –36 nm) among **1a–f**.

Time-dependent density functional theory (TD-DFT) calculations of **1a–f** were carried out at the CAM-B3LYP/6-31G(d) level of theory (Table S1, Fig. S9). Molecular geometries were adopted based the structures obtained from the X-ray diffraction analyses of the corresponding single crystals.[11] The LUMO of **1a–f** is mainly located on the benzothiadiazole ring. Meanwhile, the distribution of the HOMO orbital depends on the conformational structure and the bend angle of **1a–f**. With increasing planarity, the HOMO orbital spreads from the phenanthroimidazole to the benzothiadiazole ring and the adjacent benzene ring. When the benzothiadiazole ring exhibits a bent structure, the HOMO is mainly located on the phenanthroimidazole ring. The calculated absorption wavelengths of **1a–f** (**1a**: 369 nm; **1b**: 361 nm; **1c**: 406 nm; **1d**: 377 nm; **1e**: 349 nm; **1f**: 373 nm) should provide insights into the relationship between the molecular structures and the emission maxima. The most planar derivative **1c** showed the highest calculated absorption wavelength, whereas that of **1e**, which contains the most distorted benzothiadiazole ring, exhibits the shortest. In fact, the solid-state absorption spectra of **1a–f**, obtained by measuring diffuse reflectance spectra, revealed that in the crystalline state, **1c** and **1e** exhibit the most bathochromically or hypsochromically shifted absorptions, respectively (Fig. S11), even though the maximum absorption wavelengths of **1a–f** in solution were observed in the same region (Table 1 and Fig. S12). An optimization of the molecular structures of **1a–f** was also carried out by DFT calculations at the CAM-B3LYP/6-31G(d) level of theory, using the single-crystal X-ray diffraction structures as the initial geometry (Table S2). Dihedral angles (a–c) of the optimized structures are in the same region (a+b+c = 165.96–173.88°) and the benzothiadiazole rings of them are almost planar (bend angle <3°), indicating that the alteration of the substituent should have negligible influence on the molecular conformation of **1a–f** in the absence of crystal-packing effect. In addition, the absorption wavelengths of optimized structures obtained by TD-DFT calculations at the same level of theory are observed in a narrower region (λ_{abs} = 368–380 nm; Table S3) compared to those of X-ray structures (λ_{abs} = 349–406 nm; Table 2). These results support the notion that the molecular geometry rather than the electronic nature of the

Table 2 Sum of the dihedral angles (a–c) of adjacent (hetero)aryl groups, bend angles of the benzothiadiazole rings, and calculated maximum absorption wavelengths of **1a–f**, based on their molecular structure in the crystalline state.

Compd.	$\Delta\lambda_{em}$ (nm)[a]	a+b+c (°)[b]	Bend angle (°)[c]	Calcd. λ_{abs} (nm)[d]
1a	−11	170.55	4.61	369
1b	+7	212.19	7.19	361
1c	+58	125.84	3.28	406
1d	+4	169.74	2.57	377
1e	−36	188.52	12.11	349
1f	−15	164.57	3.04	373

[a] $\Delta\lambda_{em} = \lambda_{em}$(crystal) $-\Delta\lambda_{em}$(toluene). [b] Sum of the dihedral angles a–c (Fig. 2). [c] Bend angles of the benzothiadiazole rings (Fig. S8). [d] Maximum absorption wavelength calculated at the CAM-B3LYP/6-31G(d) level of theory.

substituent R determine the emission wavelengths of **1a–f** in the crystalline state.

Given that **1a–f** exhibit high fluorescence quantum yields both in solution and in the crystalline state, their mechano-responsive properties were subsequently examined by grinding crystalline samples with a spatula (Fig. 3 and S13). Upon strong grinding, the emission color of crystalline **1a** (R = H) bathochromically shifted by 39 nm from green (λ_{em} = 526 nm; Φ_F = 0.60) to orange (λ_{em} = 565 nm; Φ_F = 0.54). The original emission color was restored upon heating. The other derivatives **1b–f**, except for **1c**, also exhibited bathochromic shifts of the emission maxima upon grinding, and the original emission color of the ground samples was recovered upon heating. Conversely, the maximum emission wavelength of red-emissive **1c** (λ_{em} = 607 nm; Φ_F = 0.33) was hypsochromically shifted to 581 nm (Φ_F = 0.67) upon grinding. The original emission color was restored by recrystallization of ground **1c** from toluene. It should be noted that all derivatives **1a–f** exhibit yellow emission (λ_{em} = 565–581 nm) with high fluorescence quantum yields (Φ_F = 0.54–0.72) after grinding.

A powder X-ray diffraction (PXRD) analysis of **1a** revealed that the intense peaks of the powdered crystalline sample of **1a** almost disappeared upon grinding (Fig. 4b and c). The diffraction patterns of **1b–f** also significantly decreased after grinding (Fig. 4g, 4h, and S14). These results indicate that the mechano-responsive emission-color change of **1a–f** should be attributed to the phase transitions of the crystalline samples to amorphous states. In addition, the emission from amorphous **1a–f** is in the same region as that of their toluene solutions, while crystalline samples exhibit different emission colors due to crystal-packing effects. Accordingly, the substituent-dependent bathochromically or hypsochromically shifted MCL of **1a–f** should be rationalized as follows (Fig. 5): The bathochromic shift of the emission upon amorphization could be ascribed to the relaxation of the twisted or bend structure that originates from the tight crystal packing. On the other hand, crystalline **1c** adopts a planer structure due to the tight crystal packing. Upon amorphization, the molecular structure of **1c** would become more twisted, which should result in a hypsochromic shift of the emission wavelength.

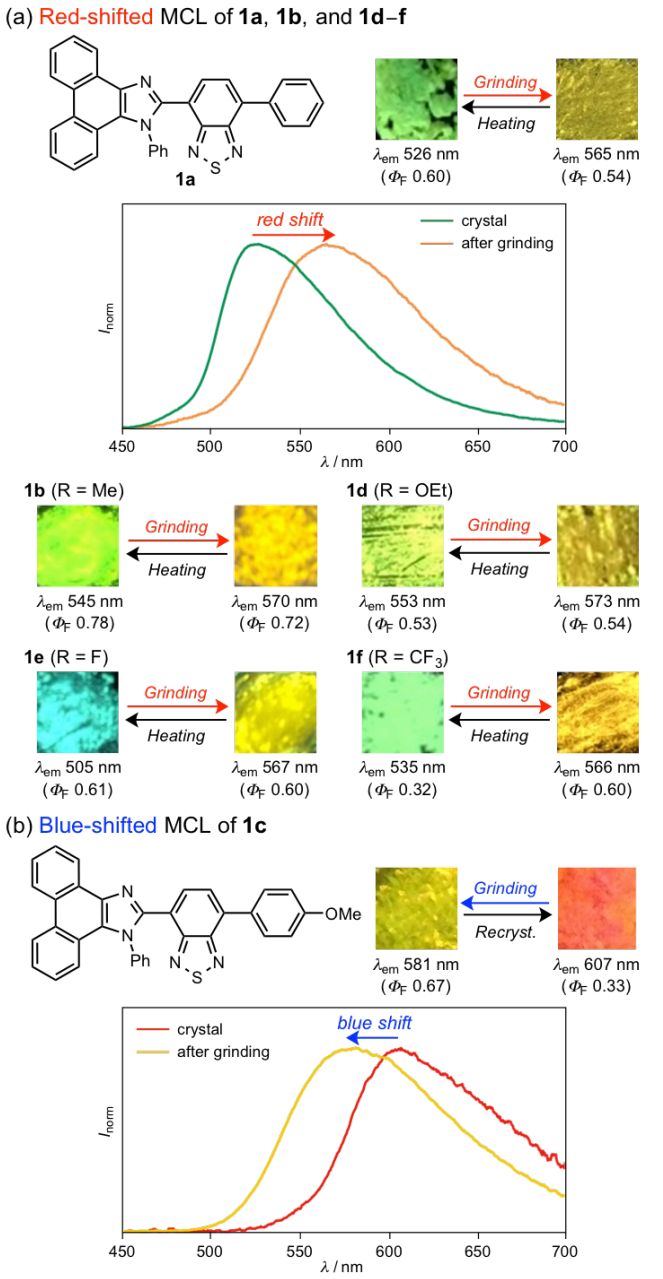

Fig. 3 Photographs and fluorescence spectra for the red-shifted MCL of **1a**, **1b**, **1d–f** (a) and the blue-shifted MCL of **1c** (b). For the fluorescence spectra for the MCL of **1b** and **1d–f**, see Fig. S13.

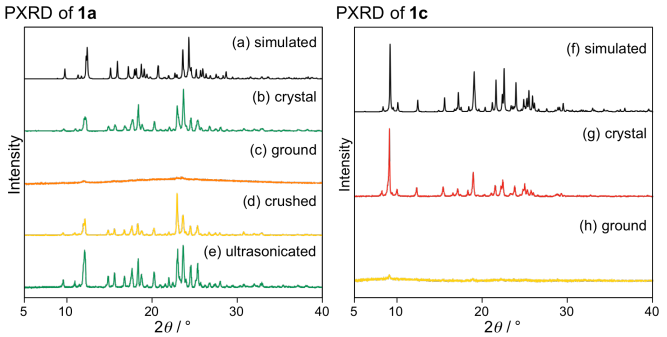

Fig. 4 PXRD patterns of **1a** and **1c**. (a,f) Simulated patterns calculated from the single-crystal X-ray diffraction structures. (b,g) Experimental patterns of the powdered crystalline samples before grinding. (c,h) Experimental patterns of the amorphous samples after grinding. (d) Experimental patterns of the crushed crystalline samples. (e) Experimental pattern of the powdered crystalline sample after ultrasonication of the crushed powder.

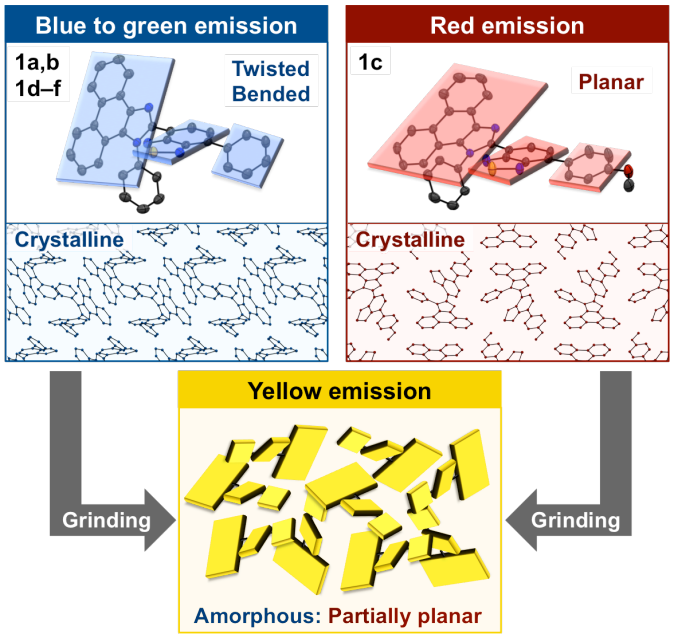

Fig. 5 Schematic representation of the mechanism of the red-shifted or blue-shifted MCL of **1a–f**.

The thermal behavior of **1a–f** was analyzed by differential scanning calorimetry (DSC) measurements (Fig. 6 and S15). The DSC thermograms of crystalline powders of **1a–f** showed only one endothermic peak that corresponds to the melting points (T_m; **1a**: 231 °C; **1b**: 225 °C; **1c**: 206 °C; **1d**: 233 °C; **1e**: 290 °C; **1f**: 245 °C), whereas cold-crystallization transition peaks from the amorphous to the crystalline state were observed for the ground samples (T_c; **1a**: 50 °C; **1b**: 134 °C; **1c**: 134 °C; **1d**: 114 °C; **1e**: 108 °C; **1f**: 149 °C). On heating ground samples of **1a–f** to their T_c, the emission colors retro-converted into the original color except for **1a** and **1c**. Non-substituted **1a** required higher temperatures (ca. 180 °C) than T_c (50 °C; Fig. 6a) to recover the original green emission, even though the emission color changed to yellow after heating to 50 °C. As discussed above, recrystallization is required for **1c** to recover

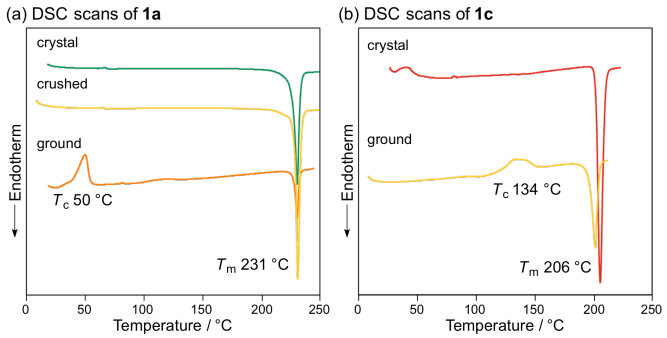

Fig. 6 (a) DSC scans for crystalline, crushed, and ground samples of **1a**. (b) DSC scans for crystalline and ground samples of **1c**. T_c and T_m values are noted near the corresponding peaks.

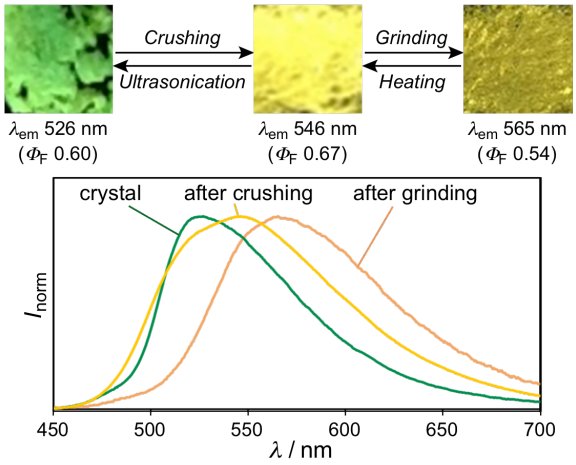

Fig. 7 Photographs and fluorescence spectra for the tricolor MCL of **1a**.

the original red emission, despite the fact that **1c** shows a T_c of 134 °C (Fig. 6b). This result suggests that high levels of crystallinity are indispensable for the red emission of **1c**.

Interestingly, when crystalline **1a** was crushed into a fine powder by weakly grinding using a spatula, the emission color changed to yellow (λ_{em} = 546 nm; Φ_F = 0.67). The original green emission was restored by heating the fine powder to 180 °C or by exposing a suspension of the fine powder in hexane to ultrasonication. On the other hand, upon strong grinding using a spatula, the yellow-emissive fine powder changed to an orange-emissive amorphous state, which is the same state as shown in Fig. 3a. Therefore, **1a** exhibited a two-step tricolor MCL from green to yellow and orange (Fig. 7). A PXRD analysis of the yellow-emissive crushed powder revealed the existence of the same crystal structure as the original green-emissive state, although the ratios of the intensity of some peaks are different between two states (Fig. 4d). Powder patterns of the green-emissive powder obtained after ultrasonication were also in good agreement with those of the original green-emissive crystals (Fig. 4e). In the DSC thermogram of the yellow-emissive crushed powder, only an endothermic peak that corresponds to the melting point (T_m = 231 °C) was observed (Fig. 6a). These results suggest that the yellow-emissive crushed powder was in a crystalline state that

exhibits considerable lattice defects, which should be responsible for the yellow emission.

In order to exclude the possibility that the yellow-emissive state is simply a mixture of two states that exhibit green and orange emission, the emission properties of the three states of the tricolor MCL of **1a** were observed at the single-particle level using fluorescence microscopy. The maximum emission wavelengths of the green-emissive crystalline (λ_{em} = 525 nm) and orange-emissive amorphous samples (λ_{em} = 578 nm) (Fig. 8a and c) were almost identical to those of their bulk samples (λ_{em}^{bulk} = 526 and 565 nm, respectively). In both cases, the lifetime delay curves fit well to a single-exponential function, with fluorescence lifetimes (τ) of 4.5 and 5.6 ns, respectively (Table 3, Fig. S16a). The single-particle-level observation revealed that the emission properties of the yellow-emissive crushed sample (λ_{em}^{bulk} = 546 nm) varied depending on different particles or surface positions. The different emission properties can be classified into three states, which exhibit green (crushed 1: λ_{em} = 538 nm), yellow (crushed 2: λ_{em} = 550 nm), and orange (crushed 3: λ_{em} = 572 nm) emission (Fig. 8b and S16b). The major component (coefficient a_1 = 0.92) of the green emissive state (crushed 1) exhibits a fluorescence lifetime of 4.4 ns, indicating that crushed 1 is almost identical to the crystalline sample (λ_{em}^{bulk} = 526 nm). Crushed 2 and 3 are composed of two components with different lifetimes [crushed 2: τ_1 = 2.6 ns (a_1 = 0.68), τ_2 = 5.7 ns (a_2 = 0.32); crushed 3: τ_1 = 3.0 ns (a_1 = 0.47), τ_2 = 6.4 ns (a_2 = 0.53)]. Notably, a rise component was clearly observed in the long-wavelength region of crushed 3 when measuring the fluorescence lifetime using bandpass filters (Fig. 8d and Table 4). The rise time (τ_1 = 0.44 ns) in the long-wavelength region (633–653 nm) of crushed 3 was close to the fast decay time (τ_1 = 0.20 ns) in the short-wavelength region (499.5–524.5 nm). Therefore, the energy transfer should occur from the crystalline to the amorphous regions, which is reasonable given that these small particles (crushed 3) were located on the surface of the larger green-emissive particles (crushed 1). In contrast, no energy transfer was observed for crushed 2, which contains two components (τ_1 = 2.5 ns, τ_2 = 5.0 ns) in the short-wavelength region and one component (τ_1 = 5.8 ns) in the long-wavelength region. These results suggest that the yellow-emissive component (τ = ca. 2.5 ns) is clearly different from those of the crystalline (τ = ca. 4.5 ns) and amorphous (τ = ca. 6.0 ns) components, and therefore we assume that this component should be assigned to the emission from the lattice defects of crystalline **1a**.

The fluorescence lifetimes of **1b–f** in the crystalline and ground states were also measured at the single-particle level using fluorescence microscopy (Table S4 and Fig. S17–21). The radiative (k_r) and non-radiative rate constants (k_{nr}) of **1a–f**, calculated from Φ_F and the mean fluorescence lifetime ($<\tau>$), are summarized, together with λ_{em} and $<\tau>$ obtained from fluorescence microscopy, in Table 5. All ground samples exhibit similar $<\tau>$, k_r, and k_{nr} values, supporting the notion that the emission properties of the ground samples are governed by the surrounding amorphous environments rather than by the nature of the substituent R. The k_r values of **1a–f**, except for that of **1c**, decrease upon amorphization, and the smallest k_r value, which was observed for crystalline **1c** probably due to the stabilization of the excited state, would account for its relatively inefficient emission (Φ_F = 0.33). Moreover, the relatively low fluorescence quantum yield of **1f** (Φ_F = 0.32) was attributed to the large k_{nr} value, which would arise from a non-radiative deactivation of the excited state on account of the thermal vibration of the trifluoromethyl group.

Table 3 Maximum fluorescence wavelengths (λ_{em}) and lifetimes (τ) for the three states of **1a** measured by single-particle-level observation using fluorescence microscopy.

Sample	λ_{em}^{bulk} (nm)	λ_{em} (nm)	τ (ns)[a]
Crystalline	526	525	4.5
Crushed	546	538	4.4 (0.92), 9.6 (0.08)
		550	2.6 (0.68), 5.7 (0.32)
		572	3.0 (0.47), 6.4 (0.53)
Ground	565	578	5.6

[a] The coefficient a_n of the component is shown in parentheses.

Table 4 Fluorescence decay and rise times for the two states of crushed **1a** in the short- and long-wavelength regions.

Sample[a]	Region (nm)	τ_1 (ns)	τ_2 (ns)	τ_3 (ns)
Crushed 2	499.5–524.5	2.5	5.0	
	633–653	5.8		
Crushed 3	499.5–524.5	0.20	1.6	4.2
	633–653	0.44	1.6	6.4

[a] Crushed 2 and 3 exhibit maximum emission wavelengths at 550 and 572 nm, respectively.

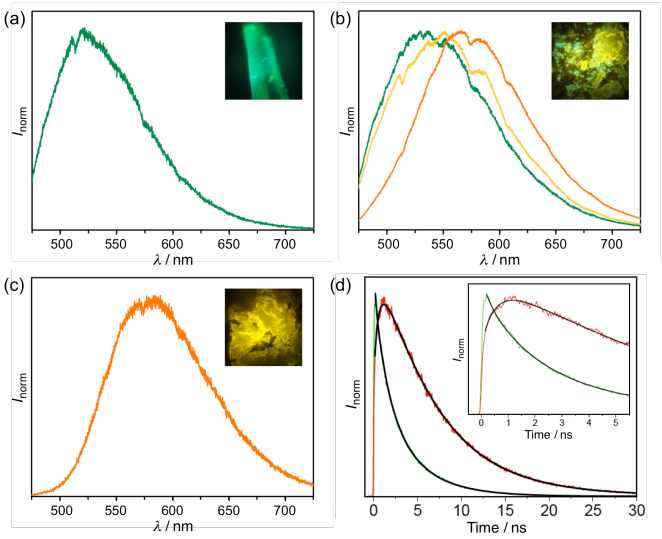

Fig. 8 Fluorescence spectra and photographs (inset) of crystalline (a), crushed 1–3 (b), and ground (c) **1a** recorded at the single-particle level. (d) Fluorescence decay profiles of crushed 3 obtained by using bandpass filters [green line: short-wavelength region (499.5–524.5 nm); red line: long-wavelength region (633–653 nm)]. The black lines indicate multiexponential curves fitted to the time profiles.

Table 5 Maximum fluorescence wavelengths (λ_{em}), mean fluorescence lifetimes ($<\tau>$) as well as radiative (k_r) and non-radiative rate constants (k_{nr}) of **1a–f** in the crystalline and ground states recorded at the single-particle level.[a]

Compd.	State	λ_{em} (nm)	$<\tau>$[b] (ns)	k_r (10^8 s^{-1})	k_{nr} (10^8 s^{-1})
1a	Crystalline	525	4.5	1.3	0.9
	Ground	578	5.6	1.0	0.8
1b	Crystalline	546	5.0	1.6	0.4
	Ground	587	5.6	1.3	0.5
1c	Crystalline	613	4.2	0.8	1.6
	Ground	586	5.8	1.2	0.6
1d	Crystalline	551	2.6	2.1	1.8
	Ground	591	5.4	1.0	0.9
1e	Crystalline	515	5.0	1.2	0.8
	Ground	589	6.0	1.0	0.7
1f	Crystalline	531	3.2	1.0	2.1
	Ground	587	6.3	0.9	0.6

[a] k_f and k_{nr} were calculated from $\Phi_F = k_f/(k_f + k_{nr}) = <\tau>k_f$. [b] Intensity-weighted mean fluorescence lifetime.

Conclusion

In summary, phenanthroimidazolylbenzothiadiazoles **1a–f**, which contain different substituents on the phenyl group at the *p*-position of the benzothiadiazole ring, were readily synthesized in high yield using a two-step procedure from commercially available starting materials. The new non-AIE-type fluorophores **1a–f** exhibit high fluorescence quantum yields both in solution and in the solid state. Single-crystal X-ray diffraction analyses and TD-DFT calculations revealed that the emission wavelengths of crystalline **1a–f** depend on their molecular geometries instead of the electronic nature of their substituents. These solid-state emissive dyes exhibit typical bathochromically shifted MCL, as well as rare tricolor MCL and hypsochromically shifted MCL. Specifically, the emission color of **1a** changes from green to yellow and orange in response to mechanical stimuli of different intensity, while that of red-emissive **1c** hypsochromically shifts to yellow upon grinding. Based on the PXRD and DSC analyses, the mechanism of the emission-color change for the bicolor MCL of **1b–f** was attributed to typical crystal-to-amorphous transitions. In the case of the tricolor MCL of **1a**, there should be another state in addition to the crystalline and amorphous states. In this study, single-particle-level observation by fluorescence microscopy has been used for the first time as an effective method for the analysis of a tricolor MCL system. The three constituent states of **1a** in the tricolor MCL could be clearly distinguished by fluorescence microscopy. We propose that the different emission properties of the lattice defects from crystalline and amorphous states should be responsible for the tricolor MCL of **1a**. In the amorphous state after grinding, almost the same emission properties (λ_{em}, Φ_F, τ, k_r, k_{nr}) were observed for all derivatives. The introduction of different substituents affords different crystal structures, which leads to the expression of versatile MCL properties. In other words, MCL properties of organic fluorophores should be easily altered by the steric effects of substituents rather than their electronic effects. This insight should provide future design guidelines for the development of new MCL dyes.

Experimental

General

All air-sensitive experiments were carried out under an atmosphere of argon unless otherwise noted. IR spectra were recorded on a Nicolet iS10 FT-IR spectrometer. ^{1}H and ^{13}C NMR spectra were recorded on a Bruker DRX-500 spectrometer using tetramethylsilane as an internal standard. Fluorescence and UV-vis absorption spectra were measured on a JASCO FP-8300 fluorescence spectrometer. For the measurement of UV-vis absorption spectra in toluene, a FUV-803 absorbance measurement cell block was used. The solid-state absorption spectra were obtained by measuring diffuse reflectance spectra using a FPA-810 powder sample cell block. The absolute fluorescence quantum yields were determined using a 100 mm ϕ integrating sphere JASCO ILF-835. A miniature fiber-optic spectrometer (FLAME-S-XR1-ES, Ocean Optics) was used for the measurements of mechanochromic luminescence. PXRD measurements were performed on a Rigaku SmartLab system using CuKα radiation. Melting points were determined on a Stuart melting point apparatus SMP3 and are uncorrected. DSC data were recorded on a Seiko Instruments DSC-6100 equipped with a liquid nitrogen cooling unit (heating rate: 10 °C min^{-1}). High-resolution electrospray ionization (HRMS-ESI) mass spectra were recorded on a Hitachi Nano Frontier LD spectrometer. TLC analyses were carried out on silica-gel 60 F_{254}-precoated aluminum-backed sheets (E. Merck). Silica gel 60 N (spherical, neutral, 63–210 mm) was used for column chromatography. Preparative TLC separations were performed on silica-gel-coated plates (Wakogel B-5F, 20 × 20 cm^2). The spectroscopic grade toluene for UV-vis absorption and fluorescence measurements was purchased from Wako Pure Chemical Industries, Ltd. and used as received.

Synthesis of 4-bromo-7-(1-phenyl-1*H*-phenanthro[9,10-*d*]imidazol-2-yl)benzo[*c*][1,2,5]thiadiazole (2)

To a solution of 7-bromobenzo[*c*][1,2,5]thiadiazole-4-carbaldehyde (74.2 mg, 0.30 mmol) and aniline (42.5 mg, 0.45 mmol) in acetic acid (4.0 mL) were added 9,10-phenanthrenequinone (63.7 mg, 0.30 mmol) and ammonium acetate (106.2 mg, 1.50 mmol). After the mixture was stirred for 12 h at 110 °C, a saturated aqueous solution of $NaHCO_3$ and dichloromethane were added to the mixture. The organic layer was separated, and the aqueous layer was extracted three times with dichloromethane. The combined organic layer was washed with water and brine, dried over anhydrous Na_2SO_4, and filtered. After removal of the solvent under reduced pressure, the crude product was purified by column chromatography on silica gel (dichloromethane/toluene = 3:1) to give 4-bromo-7-(1-phenyl-1*H*-phenanthro[9,10-*d*]imidazol-

2-yl)benzo[*c*][1,2,5]thiadiazole (**2**: 116.0 mg, 75%) as a yellow solid.

4-Bromo-7-(1-phenyl-1*H*-phenanthro[9,10-*d*]imidazol-2-yl)benzo[*c*][1,2,5]thiadiazole (2). Yellow solid; M.p. 264.0–264.3 °C; IR (KBr): ν_{max} 1497, 1451, 1396, 1320, 1194, 939, 880, 853, 757, 726 cm^{-1}; ^1H NMR (500 MHz, $CDCl_3$): δ (ppm) 8.84 (d, J = 8.1, 1H), 8.79 (d, J = 8.5 Hz, 1H), 8.72 (d, J = 8.1 Hz, 1H), 7.81 (d, J = 7.7 Hz, 1H), 7.73 (t, J = 8.1, 1H), 7.67 (t, J =8.1 Hz, 1H), 7.59 (d, J = 7.7 Hz, 1H), 7.54 (t, J =8.5 Hz, 1H), 7.49–7.47 (m, 2H), 7.44–7.39 (m, 3H), 7.30–7.26 (m, 1H), 7.25–7.24 (m, 1H); ^{13}C NMR (126 MHz, $CDCl_3$): δ (ppm) 153.24, 153.22, 147.0, 137.8, 137.7, 132.4, 131.5, 129.7, 129.6 (3C), 128.8 (2C), 128.4, 128.2, 127.4, 127.1, 126.4, 125.8, 125.3, 124.2, 123.9, 123.1, 122.8 (2C), 121.0, 115.9; HRMS-ESI (m/z): $[M + H]^+$ calcd for $C_{27}H_{16}BrN_4S$, 507.0274; found, 507.0273.

Synthesis of phenanthroimidazolylbenzothiadiazole derivatives 1a–f

Representative experimental procedure (1a, Scheme 1). A mixture of phenylboronic acid (31.7 mg, 0.26 mmol) and bromide **2** (101.2 mg, 0.20 mmol) in a mixture of toluene (2.5 mL) and an aqueous solution of K_2CO_3 (0.4 mL, 1.4 M) was degassed under ultrasonication. $Pd(PPh_3)_4$ (1.9 mg, 0.008 mmol) was added to the mixture, which was further degassed under ultrasonication. After the mixture was stirred at 110 °C for 18 h, water and dichloromethane were added to the mixture. The organic layer was separated, and the aqueous layer was extracted three times with dichloromethane. The combined organic layer was washed with water and brine, dried over anhydrous Na_2SO_4, and filtered. After removal of the solvent under reduced pressure, the crude product was purified by preparative thin-layer chromatography (dichloromethane/toluene = 9:1) to give 4-phenyl-7-(1-phenyl-1*H*-phenanthro[9,10-*d*]imidazol-2-yl)benzo[*c*][1,2,5]thiadiazole (**1a**: 78.3 mg, 79%) as a yellow solid.

4-Phenyl-7-(1-phenyl-1*H*-phenanthro[9,10-*d*]imidazol-2-yl)benzo[*c*][1,2,5]thiadiazole (1a).

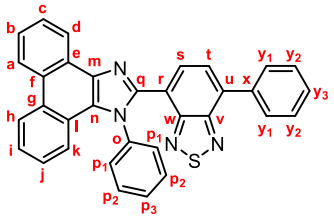

Yellow solid; M.p. 228.8–229.6 °C; IR (KBr): ν_{max} 1559, 1541, 1508, 1457, 1387, 1159, 1040, 884, 859, 756 cm^{-1}; ^1H NMR (500 MHz, $CDCl_3$): δ (ppm) 8.88 (d, J = 8.0 Hz, 1H, H*d*), 8.79 (d, J = 8.5 Hz, 1H, H*h*), 8.73 (d, J = 8.0 Hz, 1H, H*a*), 7.92–7.90 (m, 2H, Hy_1), 7.79 (d, J = 7.3 Hz, 1H, H*s*), 7.73 (t, J = 8.0 Hz, 1H, H*c*), 7.68–7.65 (m, 2H, H*b*, H*t*), 7.55–7.51 (m, 5H, H*i*, Hp_1, Hy_2), 7.47–7.44 (m, 1H, Hy_3), 7.43–7.38 (m, 3H, Hp_2, Hp_3), 7.30–7.27 (m, 2H, H*j*, H*k*); ^{13}C NMR (126 MHz, $CDCl_3$): δ (ppm) 154.4 (C*w*), 153.3 (C*v*), 148.0 (C*q*), 137.9 (C*o*), 137.8 (C*m*), 136.8 (C*x*), 135.5 (C*u*), 132.3 (C*s*), 129.50 (C*g*), 129.47 (Cp_2,Cp_3), 129.3 (Cy_1), 128.9 (Cp_1), 128.7 (Cy_3), 128.6 (Cy_2), 128.4 (C*f*), 128.1 (C*n*), 127.31 (C*e*), 127.25 (C*c*), 127.1 (C*t*), 126.3 (C*j*), 125.7 (C*b*), 125.2 (C*i*), 124.1 (C*h*), 123.1 (C*a, Cr*), 122.91 (C*l*), 122.89 (C*d*), 121.0 (C*k*); HRMS-ESI (m/z): $[M + H]^+$ calcd for $C_{33}H_{21}N_4S$, 505.1482; found, 505.1483. Crystal data for **1a** (CCDC 1886938): $C_{33}H_{20}N_4S$, M = 504.61, monoclinic, a = 11.56239(16) Å, b = 10.33576(16) Å, c = 20.3081(3) Å, β = 95.3214(12)°, V = 2416.48(6) $Å^3$, space group $P2_1/c$ (no. 14), Z = 4, D_c = 1.387 g cm^{-3}, F(000) = 1048.00, T = 223(1) K, μ(Cu-Kα) = 14.302 cm^{-1}, 35863 reflections measured, 4434 independent (R_{int} = 0.0694). The final refinement converged to R_1 = 0.0426 for $I > 2.0\sigma(I)$, wR_2 = 0.1157 for all data.

4-(1-Phenyl-1*H*-phenanthro[9,10-*d*]imidazol-2-yl)-7-(*p*-tolyl)benzo[*c*][1,2,5]thiadiazole (1b). Yellow solid; M.p. 222.7–224.1 °C; IR (KBr): ν_{max} 1496, 1472, 1450, 1387, 1321, 882, 819, 752, 723, 709 cm^{-1}; ^1H NMR (500 MHz, $CDCl_3$): δ (ppm) 8.87 (d, J = 8.2 Hz, 1H), 8.80 (d, J = 8.5 Hz, 1H), 8.73 (d, J = 8.2 Hz, 1H), 7.81 (d, J = 7.9 Hz, 2H), 7.77 (d, J = 7.3 Hz, 1H), 7.73 (t, J = 8.2 Hz, 1H), 7.68–7.63 (m, 2H), 7.55–7.53 (m, 3H), 7.43–7.39 (m, 3H), 7.33 (d, J = 7.9 Hz, 2H), 7.30–7.26 (m, 2H), 2.44 (s, 3H); ^{13}C NMR (126 MHz, $CDCl_3$): δ (ppm) 154.4, 153.4, 148.0, 138.8, 138.0, 137.8, 135.5, 134.0, 132.3, 129.46, 129.45 (3C), 129.3 (2C), 129.2 (2C), 128.9 (2C), 128.3, 128.1, 127.28, 127.26, 126.7, 126.3, 125.7, 125.1, 124.1, 123.1, 122.91, 122.89, 122.7, 121.0, 21.28; HRMS-ESI (m/z): $[M + H]^+$ calcd for $C_{34}H_{23}N_4S$, 519.1638; found, 519.1636. Crystal data for **1b** (CCDC 1886939): $C_{34}H_{22}N_4S$, M = 518.64, triclinic, a = 11.68960(7) Å, b = 15.16518(10) Å, c = 16.54421(10) Å, α = 106.7151(6)°, β = 97.5581(5)°, γ = 110.4272(6)°, V = 2542.92(3) $Å^3$, space group P-1 (no. 2), Z = 4, D_c = 1.355 g cm^{-3}, F(000) = 1080.00, T = 223(1) K, μ(Cu-Kα) = 13.734 cm^{-1}, 61336 reflections measured, 9290 independent (R_{int} = 0.0741). The final refinement converged to R_1 = 0.0461 for $I > 2.0\sigma(I)$, wR_2 = 0.1301 for all data.

4-(4-Methoxyphenyl)-7-(1-phenyl-1*H*-phenanthro[9,10-*d*]imidazol-2-yl)benzo[*c*][1,2,5]thiadiazole (1c). Orange solid; M.p. 204.2–206.2 °C; IR (KBr): ν_{max} 1607, 1515, 1497, 1247, 1187, 1040, 890, 828, 759, 701 cm^{-1}; ^1H NMR (500 MHz, $CDCl_3$): δ (ppm) 8.87 (d, J = 8.3 Hz, 1H), 8.80 (d, J = 8.5 Hz, 1H), 8.73 (d, J = 8.3 Hz, 1H), 7.91–7.89 (m, 2H), 7.77 (d, J = 7.3 Hz, 1H), 7.73 (t, J = 8.3 Hz, 1H), 7.66 (t, J = 8.3 Hz, 1H), 7.61 (d, J = 7.3 Hz, 1H), 7.55–7.53 (m, 3H), 7.45–7.39 (m, 3H), 7.30–7.25 (m, 2H), 7.06–7.05 (m, 2H), 3.88 (s, 3H); ^{13}C NMR (126 MHz, $CDCl_3$): δ (ppm) 160.2, 154.4, 153.4, 148.1, 138.0, 137.8, 135.1, 132.4, 130.6 (2C), 129.5 (4C), 129.3, 128.9 (2C), 128.4, 128.1, 127.3 (2C), 126.3, 126.2, 125.7, 125.1, 124.1, 123.1, 122.94, 122.91, 122.4, 121.1, 114.1 (2C), 55.4; HRMS-ESI (m/z): $[M + H]^+$ calcd for $C_{34}H_{23}N_4OS$, 535.1587; found, 535.1597. Crystal data for **1c**

(CCDC 1886940): $C_{34}H_{22}N_4OS$, M = 534.63, orthorhombic, a = 19.24398(15) Å, b = 21.13245(17) Å, c = 6.19786(5) Å, V = 2520.50(3) Å^3, space group $Pna2_1$ (no. 33), Z = 4, D_c = 1.409 g cm^{-3}, F(000) = 1112.00, T = 223(1) K, μ(Cu-Kα) = 14.341 cm^{-1}, 15869 reflections measured, 3641 independent (R_{int} = 0.0358). The final refinement converged to R_1 = 0.0309 for $I > 2.0\sigma(I)$, wR_2 = 0.0814 for all data.

4-(4-Ethoxyphenyl)-7-(1-phenyl-1*H*-phenanthro[9,10-*d*]imidazol-2-yl)benzo[*c*][1,2,5]thiadiazole (1d). Yellow solid; M.p. 232.6–233.6 °C; IR (KBr): ν_{max} 1606, 1497, 1472, 1387, 1252, 1044, 886, 835, 758, 707 cm^{-1}; ^{1}H NMR (500 MHz, $CDCl_3$): δ (ppm) 8.87 (d, J = 8.0 Hz, 1H), 8.79 (d, J = 8.5 Hz, 1H), 8.72 (d, J = 8.0 Hz, 1H), 7.90–7.88 (m, 2H), 7.77 (d, J = 7.3 Hz, 1H), 7.73 (t, J = 8.0 Hz, 1H), 7.66 (t, J = 8.0 Hz, 1H), 7.61 (d, J = 7.3 Hz, 1H), 7.55–7.52 (m, 3H), 7.42–7.37 (m, 3H), 7.30–7.25 (m, 2H), 7.05–7.02 (m, 2H), 4.11 (q, J = 7.0 Hz, 2H), 1.45 (t, J = 7.0 Hz, 3H); ^{13}C NMR (126 MHz, $CDCl_3$): δ (ppm) 159.6, 154.5, 153.4, 148.2, 138.1, 137.8, 135.2, 132.4, 130.6 (2C), 129.5, 129.4 (3C), 129.2, 129.0 (2C), 128.4, 128.1, 127.33, 127.28, 126.3, 126.1, 125.7, 125.1, 124.1, 123.1, 123.0, 122.9, 122.4, 121.1, 114.7 (2C), 63.6, 14.8; HRMS-ESI (m/z): [M + H]$^+$ calcd for $C_{35}H_{25}N_4OS$, 549.1744; found, 549.1744. Crystal data for **1d** (CCDC 1886941): $C_{35}H_{24}N_4OS$, M = 548.66, monoclinic, a = 15.39674(12) Å, b = 10.80897(7) Å, c = 17.32088(15) Å, β = 105.4259(9)°, V = 2778.75(4) Å^3, space group $P2_1/n$ (no. 14), Z = 4, D_c = 1.311 g cm^{-3}, F(000) = 1144.00, T = 223(1) K, μ(Cu-Kα) = 13.140 cm^{-1}, 34979 reflections measured, 5081 independent (R_{int} = 0.0585). The final refinement converged to R_1 = 0.0435 for $I > 2.0\sigma(I)$, wR_2 = 0.1215 for all data.

4-(4-Fluorophenyl)-7-(1-phenyl-1*H*-phenanthro[9,10-*d*]imidazol-2-yl)benzo[*c*][1,2,5]thiadiazole (1e). Yellow solid; M.p. 228.8–229.6 °C; IR (KBr): ν_{max} 1599, 1496, 1388, 1321, 1215, 1163, 883, 833, 761, 699 cm^{-1}; ^{1}H NMR (500 MHz, $CDCl_3$): δ (ppm) 8.87 (d, J = 8.1 Hz, 1H), 8.80 (d, J = 8.5 Hz, 1H), 8.73 (d, J = 8.1 Hz, 1H), 7.92–7.89 (m, 2H), 7.79 (d, J = 7.3 Hz, 1H), 7.73 (t, J = 8.1 Hz, 1H), 7.67 (t, J = 8.1 Hz, 1H), 7.63 (d, J = 7.3 Hz, 1H), 7.56–7.53 (m, 3H), 7.44–7.40 (m, 3H), 7.30–7.26 (m, 2H), 7.23–7.20 (m, 2H); ^{13}C NMR (126 MHz, $CDCl_3$): δ (ppm) 163.1 (d, $^1J_{C\text{-}F}$ = 249 Hz), 154.4, 153.2, 147.9, 138.0, 137.8, 134.4, 132.9 (d, $^4J_{C\text{-}F}$ = 2.7 Hz), 132.3, 131.1 (d, $^3J_{C\text{-}F}$ = 7.3 Hz, 2C), 129.53, 129.50 (3C), 128.9 (2C), 128.4, 128.2, 127.33, 127.25, 126.9, 126.3, 125.7, 125.2, 124.1, 123.3, 123.1, 122.91, 122.89, 121.1, 115.6 (d, $^2J_{C\text{-}F}$ = 22 Hz, 2C); HRMS-ESI (m/z): [M + H]$^+$ calcd for $C_{33}H_{20}FN_4S$, 523.1387; found, 523.1387. Crystal data for **1e** (CCDC 1886942): $C_{33}H_{19}FN_4S$, M = 522.60, monoclinic, a = 9.7866(3) Å, b = 16.2397(5) Å, c = 15.7471(5) Å, β = 102.022(3)°, V = 2447.82(13) Å^3, space group $P2_1/n$ (no. 14), Z = 4, D_c = 1.418 g cm^{-3}, F(000) = 1080.00, T = 223(1) K, μ(Cu-Kα) = 14.932 cm^{-1}, 25114 reflections measured, 4474 independent (R_{int} = 0.0450). The final refinement converged to R_1 = 0.0390 for $I > 2.0\sigma(I)$, wR_2 = 0.1073 for all data.

4-(1-Phenyl-1*H*-phenanthro[9,10-*d*]imidazol-2-yl)-7-[4-(trifluoromethyl)phenyl]benzo[*c*][1,2,5]thiadiazole (1f). Yellow solid; M.p. 228.8–229.6 °C; IR (KBr): ν_{max} 1497, 1388, 1326, 1163, 1116, 1066, 885, 834, 758, 699 cm^{-1}; ^{1}H NMR (500 MHz, $CDCl_3$): δ (ppm) 8.87 (d, J = 8.1 Hz, 1H), 8.80 (d, J = 7.9 Hz, 1H), 8.74 (d, J = 8.1 Hz, 1H), 8.03 (d, J = 8.4 Hz, 2H), 7.82 (d, J = 7.3 Hz, 1H), 7.78 (d, J = 8.4 Hz, 2H), 7.74 (t, J = 8.1 Hz, 1H), 7.70 (d, J = 7.3 Hz, 1H), 7.67 (t, J = 8.1 Hz, 1H), 7.56–7.54 (m, 3H), 7.45–7.41 (m, 3H), 7.31–7.25 (m, 2H); ^{13}C NMR (126 MHz, $CDCl_3$): δ (ppm) 154.3, 153.1, 147.6, 140.3, 137.93, 137.86, 133.9, 132.1, 130.6 (q, $^2J_{C\text{-}F}$ = 33 Hz), 129.63 (2C), 129.61, 129.58, 129.56 (2C), 128.9 (2C), 128.4, 128.2, 127.7, 127.4, 127.2, 126.4, 125.8, 125.6 (q, $^3J_{C\text{-}F}$ = 3.7 Hz, 2C), 125.3, 124.22, 124.17, 124.1 (q, $^1J_{C\text{-}F}$ = 272 Hz), 123.1, 122.9 (2C), 121.1; HRMS-ESI (m/z): [M + H]$^+$ calcd for $C_{34}H_{20}F_3N_4S$, 573.1355; found, 573.1354. Crystal data for **1f** (CCDC 1886943): $C_{34}H_{19}F_3N_4S$, M = 572.61, monoclinic, a = 10.20299(16) Å, b = 15.8241(2) Å, c = 16.8045(3) Å, β = 93.1817(15)°, V = 2708.96(7) Å^3, space group Pc (no. 7), Z = 4, D_c = 1.404 g cm^{-3}, F(000) = 1176.00, T = 223(1) K, μ(Cu-Kα) = 15.097 cm^{-1}, 28440 reflections measured, 8231 independent (R_{int} = 0.0668). The final refinement converged to R_1 = 0.0633 for $I > 2.0\sigma(I)$, wR_2 = 0.1793 for all data.

Theoretical calculations

The theoretical calculations were performed using the Gaussian 16 program.[12] The six lowest singlet–singlet transitions of **1a** were calculated using time-dependent density functional theory (TD-DFT) calculations at the CAM-B3LYP/6-31G(d) level of theory. The molecular structure of **1a**, obtained from the single-crystal X-ray diffraction analysis, was used as a starting point. Here, the long-range-corrected hybrid functional CAM-B3LYP was used, as CAM-B3LYP often provides better results in TD-DFT calculations than B3LYP, which is conventionally used in DFT calculations.[13] The HOMO and LUMO energy levels of **1a** are –6.48 eV and –1.27 eV, respectively. The calculated first excited state, which consists of the transition from the HOMO to the LUMO (0.642), is 369 nm (3.36 eV) with an oscillator strength of 0.339. The theoretical calculations of **1b–f** were carried out as described for **1a** (Table S1). In the unit cells of **1b** and **1f**, two independent molecules with different molecular geometry were observed. In both cases, calculations were carried out for both structures (**1b-1** and **1b-2**; **1f-1** and **1f-2**). An optimization of the molecular structures of **1a–f** was carried out by DFT calculations at the CAM-B3LYP/6-31G(d) level of theory, using the single-crystal X-ray diffraction structures as the initial geometry. The TD-DFT calculations of the optimized structures were also performed as described for the single-crystal X-ray diffraction structures.

Single-particle-level observations

Single-particle fluorescence measurements were performed on a home-built wide-field/confocal microscope equipped with

a Nikon Ti-E inverted fluorescence microscope. The fluorescence images were recorded using an electron-multiplying charge-coupled device camera (Evolve 512, Roper Scientific) or color sCMOS camera (Dhyana 400DC, Tucsen Photonics) using Micro-Manager (https://www.micro-manager.org/). The 405-nm continuous wave laser (OBIS 405LX, Coherent) or 405-nm pulsed diode laser (PiL040X, Advanced Laser Diode System, 45-ps FWHM) was used to excite the samples. A dichroic mirror (Di02-R405, Semrock) and a longpass filter (BLP01-458R, Semrock) were used to filter the scattering from excitation light. To separate the fluorescence signals, bandpass filters (FF01-512/25, FF01-643/20, Semrock) were used. For the spectroscopy, only the emission that passed through a slit entered the imaging spectrograph (MS3504i, SOL instruments) equipped with a CCD camera (DU416A-LDC-DD, Andor). For time-resolved PL measurements, the emitted photons were passed through a 100-μm pinhole and then directed onto a single-photon avalanche diode (SPD-050, Micro Photon Devices). The signals from the detector were sent to a time-correlated single photon counting module (SPC-130EM, Becker & Hickl) for further analysis. The instrument response function of the system was about 100 ps. All the experiments were conducted at room temperature. The data were analyzed using ImageJ (http://rsb.info.nih.gov/ij/) and Origin 2018 (OriginLab).

Conflicts of interest

There are no conflicts to declare.

Acknowledgements

This work was partly supported by JSPS KAKENHI Grant Numbers 18H04508 and 18H04517 in Grant-in-Aid for Scientific Research on Innovative Areas “Soft Crystals: Area No. 2903”, by the Tonen General Research Foundation, and by the CASIO Science Promotion Foundation. The authors are grateful to Mr. Shinji Ishihara (Instrumental Analysis Center, Yokohama National University) for carrying out the HRMS-ESI analyses.

Notes and references

1 For a review on solid-state emissive organic dyes, see: M. Shimizu and T. Hiyama, *Chem.–Asian J.*, 2010, **5**, 1516.

2 For recently reported examples of solid-state emissive organic dyes, see: (a) R. Huang, B. Liu, C. Wang, Y. Wang and H. Zhang, *J. Phys. Chem. C*, 2018, **122**, 10510; (b) T. Namba, Y. Hayashi, S. Kawauchi, Y. Shibata and K. Tanaka, *Chem.–Eur. J.*, 2018, **24**, 7161; (c) B. Tang, C. Wang, Y. Wang and H. Zhang, *Angew. Chem., Int. Ed.*, 2017, **56**, 12543; (d) C. Maeda, T. Todaka, T. Ueda and T. Ema, *Chem.–Eur. J.*, 2016, **22**, 7508; (e) T. Mutai, T. Ohkawa, H. Shono and K. Araki, *J. Mater. Chem. C.*, 2016, **4**, 3599; (f) T. Beppu, K. Tomiguchi, A. Masuhara, Y.-J. Pu and H. Katagiri, *Angew. Chem., Int. Ed.*, 2015, **54**, 7332; (g) A. C. Shaikh, D. S. Ranade, S. Thorat, A. Maity, P. P. Kulkarni, R. G. Gonnade, P. Munshi and N. T. Patil, *Chem. Commun.*, 2015, **51**, 16115; (h) K. Benelhadj, W. Muzuzu, J. Massue, P. Retailleau, A. Charaf-Eddin, A. D. Laurent, D. Jacquemin, G. Ulrich and R. Ziessel, *Chem.–Eur. J.*, 2014, **20**, 12843; (i) Y. Fujiwara, R. Ozawa, D. Onuma, K. Suzuki, K. Yoza and K. Kobayashi, *J. Org. Chem.*, 2013, **78**, 2206; (j) M. Shimizu, R. Kaki, Y. Takeda, T. Hiyama, N. Nagai, H. Yamagishi and H. Furutani, *Angew. Chem., Int. Ed.*, 2012, **51**, 4095.

3 For recent reviews on MCL dyes, see: (a) Y. Sagara, S. Yamane, M. Mitani, C. Weder and T. Kato, *Adv. Mater.*, 2016, **28**, 1073; (b) Z. Ma, Z. Wang, M. Teng, Z. Xu and X. Jia, *ChemPhysChem*, 2015, **16**, 1811.

4 For seminal examples of MCL dyes, see: (a) Y. Sagara, T. Mutai, I. Yoshikawa and K. Araki, *J. Am. Chem. Soc.*, 2007, **129**, 1520; (b) J. Kunzelman, M. Kinami, B. R. Crenshaw, J. D. Protasiewicz and C. Weder, *Adv. Mater.*, 2008, **20**, 119; (c) H. Ito, T. Saito, N. Oshima, N. Kitamura, S. Ishizaka, Y. Hinatsu, M. Wakeshima, M. Kato, K. Tsuge and M. Sawamura, *J. Am. Chem. Soc.*, 2008, **130**, 10044; (d) T. Abe, T. Itakura, N. Ikeda and K. Shinozaki, *Dalton Trans.*, 2009, 711; (e) Y. Ooyama, Y. Kagawa, H. Fukuoka, G. Ito, Y. Harima, *Eur. J. Org. Chem.*, 2009, 5321; (f) G. Zhang, J. Lu, M. Sabat and C. L. Fraser, *J. Am. Chem. Soc.*, 2010, **132**, 2160; (g) S. Perruchas, X. F. L. Goff, S. Maron, I. Maurin, F. Guillen, A. Garcia, T. Gacoin and J.-P. Boilot, *J. Am. Chem. Soc.*, 2010, **132**, 10967; (h) X. Zhang, Z. Chi, H. Li, B. Xu, X. Li, W. Zhou, S. Liu, Y. Zhang and J. Xu, *Chem.–Asian J.*, 2011, **6**, 808; (i) X. Zhang, Z. Chi, J. Zhang, H. Li, B. Xu, X. Li, S. Liu, Y. Zhang and J. Xu, *J. Phys. Chem. B*, 2011, **115**, 7606; (j) S.-J. Yoon and S. Y. Park, *J. Mater. Chem.*, 2011, **21**, 8338; (k) Y. Dong, B. Xu, J. Zhang, X. Tan, L. Wang, J. Chen, H. Lv, S. Wen, B. Li, L. Ye, B. Zou and W. Tian, *Angew. Chem., Int. Ed.*, 2012, **51**, 10782; (l) K. Nagura, S. Saito, H. Yusa, H. Yamawaki, H. Fujihisa, H. Sato, Y. Shimoikeda, S. Yamaguchi, *J. Am. Chem. Soc.*, 2013, **135**, 10322; (m) M. Krikorian, S. Liu and T. M. Swager, *J. Am. Chem. Soc.*, 2014, **136**, 2952.

5 For recent reviews on AIE dyes, see: (a) Z. He, C. Ke and B. Z. Tang, *ACS Omega*, 2018, **3**, 3267; (b) M. Gao and B. Z. Tang, *ACS Sens.*, 2017, **2**, 1382; (c) J. Yang, J. Huang, Q. Li and Z. Li, *J. Mater. Chem. C*, 2016, **4**, 2663; (d) Z. Guo, A. Shao and W.-H. Zhu, *J. Mater. Chem. C*, 2016, **4**, 2640; (e) J. Mei, N. L. C. Leung, R. T. K. Kwok, J. W. Y. Lam and B. Z. Tang, *Chem. Rev.*, 2015, **115**, 11718; (f) R. Hu, N. L. C. Leung and B. Z. Tang, *Chem. Soc. Rev.*, 2014, **43**, 4494.

6 For recent examples of MCL dyes with AIE properties, see: (a) Z. Wang, Y. Li, D. Yuan, L. Qian, L. Li, H. Wu, M. Liu, J. Ding and X. Huang, *Dyes Pigm.*, 2019, **162**, 203; (b) Y. Chen, S. Wang, X. Wu, Y. Xu, H. Li, Y. Liu, H. Tong and L. Wang, *J. Mater. Chem. C*, 2018, **6**, 12503; (c) Z. Wu, S. Mo, L. Tan, B. Fang, Z. Su, Y. Zhang and M. Yin, *Small*, 2018, **14**, 1802524, (d) K. Santhiya, S. K. Sen, R. Natarajan, R. Shankar and B. Murugesapandian, *J. Org. Chem.*, 2018, **83**, 10770; (e) B. Huang, W.-C. Chen, Z. Li, J. Zhang, W. Zhao, Y. Feng, B. Z. Tang and C.-S. Lee, *Angew. Chem., Int. Ed.*, 2018, **57**, 12473; (f) T. Butler, M. Zhuang and C. L. Fraser, *J. Phys. Chem. C*, 2018, **122**, 19090; (g) H. Zhu, P. Chen, L. Kong, Y. Tian and J. Yang, *J. Phys. Chem. C*, 2018, **122**, 19793; (h) Y. Zhang, Y. Ma, L. Kong, Y. Tian and J. Yang, *Dyes Pigm.*, 2018, **159**, 314; (i) Q. Chai, J. Wei, B. Bai, H. Wang and M. Li, *Dyes Pigm.*, 2018, **152**, 93; (j) C. Ma, J. He, B. Xu, G. Xie, Z. Xie, Z. Mao and Z. Chi, *RSC Adv.*, 2018, **8**, 6252; (k) Y. Wang, D. Xu, H. Gao, Y. Wang, X. Liu, A. Han, C. Zhang and L. Zhang, *J. Phys. Chem. C*, 2018, **122**, 2297.

7 A limited number of MCL dyes with the same molecular scaffold exhibit both bathochromically and hypsochromically shifted MCL. For examples, see: (a) M. Kondo, T. Yamato, S. Miura, M. Hashimoto, C. Kitamura and N. Kawatsuki, *Chem.–Asian J.*, 2019, **14**, 471; (b) Y. Liu, Q. Zeng, B. Zou, Y. Liu, B. Xu and W. Tian, *Angew. Chem., Int. Ed.*, 2018, **57**, 15670; (c) T.

Seki, K. Kobayashi, T. Mashimo and H. Ito, *Chem. Commun.*, 2018, **54**, 11136; (d) B. Li, K. Seth, B. Niu, L. Pan, H. Yang, and H. Ge, *Angew. Chem., Int. Ed.*, 2018, **57**, 3401; (e) G. Li, Y. Xu, Q. Kong, W. Zhuang and Y. Wang, *J. Mater. Chem. C*, 2017, **5**, 8527; (f) J. Wu, Y. Cheng, J. Lan, D. Wu, S. Qian, L. Yan, Z. He, X. Li, K. Wang, B. Zou and J. You, *J. Am. Chem. Soc.*, 2016, **138**, 12803. (g) Y. Zhang, H. Mao, L. Kong, Y. Tian, Z. Tian, X. Zeng, J. Zhi, J. Shi, B. Tong, Y. Dong, *Dyes Pigm.*, 2016, **133**, 354; (h) R. Yoshii, K. Suenaga, K. Tanaka and Y. Chujo, *Chem. Eur. J.*, 2015, **21**, 7231, See also ref. 4l.

8 Little is known about MCL dyes that exhibit multicolor MCL. For examples, see: (a) S. Ito, G. Katada, T. Taguchi, I. Kawamura, T. Ubukata and M. Asami, *CrystEngComm*, 2019, **21**, 53; (b) X. Wu, J. Guo, Y. Cao, J. Zhao, W. Jia, Y. Chen and D. Jia, *Chem. Sci.*, 2018, **9**, 5270; (c) W. Yang, C. Liu, S. Lu, J. Du, Q. Gao, R. Zhang, Y. Liu and C. Yang, *J. Mater. Chem. C*, 2018, **6**, 290; (d) M. Okazaki, Y. Takeda, P. Data, P. Pander, H. Higginbotham, A. P. Monkman and S. Minakata, *Chem. Sci.*, 2017, **8**, 2677. (e) S. Ito, T. Yamada and M. Asami, *ChemPlusChem*, 2016, **81**, 1272; (f) Z. Ma, Z. Wang, X. Meng, Z. Ma, Z. Xu, Y. Ma and X. Jia, *Angew. Chem., Int. Ed.*, 2016, **55**, 519; (g) Y. Sagara and T. Kato, *Angew. Chem., Int. Ed.*, 2011, **50**, 9128.

9 (a) S. Ito, T. Taguchi, T. Yamada, T. Ubukata, Y. Yamaguchi and M. Asami, *RSC Adv.*, 2017, **7**, 16953; (b) S. Ito, T. Yamada, T. Taguchi, Y. Yamaguchi and M. Asami, *Chem.–Asian J.*, 2016, **11**, 1963.

10 For examples of optoelectronic properties of phenanthroimidazole derivatives, see: (a) N. Zhao, Y. Li, Y. Jia and P. Li, *J. Phys. Chem. C*, 2018, **122**, 26576; (b) Y. Li, W. Wang, Z. Zhuang, Z. Wang, G. Lin, P. Shen, S. Chen, Z. Zhao and B. Z. Tang, *J. Mater. Chem. C*, 2018, **6**, 5900; (c) V. Thanikachalam, P. Jeeva and J. Jayabharathi, *RSC Adv.*, 2017, **7**, 13604; (d) W.-C. Chen, Y. Yuan, S.-F. Ni, Q.-X. Tong, F.-L. Wong and C.-S. Lee, *Chem. Sci.*, 2017, **8**, 3599; (e) K. Skonieczny, J. Yoo, J. M. Larsen, E. M. Espinoza, M. Barbasiewicz, V. I. Vullev, C.-H. Lee and D. T. Gryko, *Chem. Eur. J.*, 2016, **22**, 7485; (f) K. Wang, S. Wang, J. Wei, S. Chen, D. Liu, Y. Liu and Y. Wang, *J. Mater. Chem. C*, 2014, **2**, 6817; (g) R. Francke and R. D. Little, *J. Am. Chem. Soc.*, 2014, **136**, 427; (h) Z. Gao, Y. Liu, Z. Wang, F. Shen, H. Liu, G. Sun, L. Yao, Y. Lv, P. Lu and Y. Ma, *Chem. Eur. J.*, 2013, **19**, 2602; (i) Y. Zhang, S.-L. Lai, Q.-X. Tong, M.-F. Lo, T.-W. Ng, M.-Y. Chan, Z.-C. Wen, J. He, K.-S. Jeff, X.-L. Tang, W.-M. Liu, C.-C. Ko, P.-F. Wang and C.-S. Lee, *Chem. Mater.*, 2012, **24**, 61; (j) Z. Wang, P. Lu, S. Chen, Z. Gao, F. Shen, W. Zhang, Y. Xu, H. S. Kwok and Y. Ma, *J. Mater. Chem.*, 2011, **21**, 5451.

11 Although there are two independent molecules with different geometry in the unit cells of **1b** and **1f**, only the ones with larger oscillator strength are shown in Table 2.

12 Gaussian 16, Revision A.03, M. J. Frisch, G. W. Trucks, H. B. Schlegel, G. E. Scuseria, M. A. Robb, J. R. Cheeseman, G. Scalmani, V. Barone, G. A. Petersson, H. Nakatsuji, X. Li, M. Caricato, A. V. Marenich, J. Bloino, B. G. Janesko, R. Gomperts, B. Mennucci, H. P. Hratchian, J. V. Ortiz, A. F. Izmaylov, J. L. Sonnenberg, D. Williams-Young, F. Ding, F. Lipparini, F. Egidi, J. Goings, B. Peng, A. Petrone, T. Henderson, D. Ranasinghe, V. G. Zakrzewski, J. Gao, N. Rega, G. Zheng, W. Liang, M. Hada, M. Ehara, K. Toyota, R. Fukuda, J. Hasegawa, M. Ishida, T. Nakajima, Y. Honda, O. Kitao, H. Nakai, T. Vreven, K. Throssell, J. A. Montgomery, Jr., J. E. Peralta, F. Ogliaro, M. J. Bearpark, J. J. Heyd, E. N. Brothers, K. N. Kudin, V. N. Staroverov, T. A. Keith, R. Kobayashi, J. Normand, K. Raghavachari, A. P. Rendell, J. C. Burant, S. S. Iyengar, J. Tomasi, M. Cossi, J. M. Millam, M. Klene, C. Adamo, R. Cammi, J. W. Ochterski, R. L. Martin, K. Morokuma, O. Farkas, J. B. Foresman and D. J. Fox, Gaussian, Inc., Wallingford CT, 2016.

13 D. Jacquemin, E. A. Perpète, G. E. Scuseria, I. Ciofini and C. Adamo, *J. Chem. Theory Comput.*, 2008, **4**, 123.